



Since January 2020 Elsevier has created a COVID-19 resource centre with free information in English and Mandarin on the novel coronavirus COVID-19. The COVID-19 resource centre is hosted on Elsevier Connect, the company's public news and information website.

Elsevier hereby grants permission to make all its COVID-19-related research that is available on the COVID-19 resource centre - including this research content - immediately available in PubMed Central and other publicly funded repositories, such as the WHO COVID database with rights for unrestricted research re-use and analyses in any form or by any means with acknowledgement of the original source. These permissions are granted for free by Elsevier for as long as the COVID-19 resource centre remains active.



# Highly sensitive aptasensor for the detection of SARS-CoV-2-RBD using aptamer-gated methylene blue@mesoporous silica film/laser engraved graphene electrode

Mahmoud Amouzadeh Tabrizi<sup>\*</sup>, Pablo Acedo<sup>\*\*</sup>

Electronic Technology Department, Universidad Carlos III de Madrid, Leganés, Spain

## ARTICLE INFO

### Keywords:

Aptasensor  
Electrochemical measurement  
Aptamer gated-mesoporous silica film  
SARS-CoV-2-RBD

## ABSTRACT

Herein, an aptasensor was designed to detect the receptor-binding domain of severe acute respiratory syndrome coronavirus-2 (SARS-CoV-2-RBD) based on the encapsulation of the methylene blue (MB) inside the mesoporous silica film (MPSF), and an aptamer as an electrochemical probe, a porous matrix, and a bio-gatekeeper, respectively. The signal analysis of the proposed aptasensor indicated that the surface coverage of the encapsulated MB inside the MPSF (MB@MPSF) was  $1.9 \text{ nmol/cm}^2$ . Aptamers were capped the MB@MPSF, avoiding the release of MB into the solution via the electrostatic attraction between the positively charged amino groups of the MPSF and negatively charged phosphate groups of the aptamers. Therefore, the electrochemical signal of the encapsulated MB in the absence of the SARS-CoV-2-RBD was high. In the presence of SARS-CoV-2-RBD, the aptamers that had a high affinity to the SARS-CoV-2-RBD molecules were removed from the electrode surface to interact with SARS-CoV-2-RBD. It gave rise to the release of the MB from the MPSF to the solution and washed away on the electrode surface. Therefore, the electrochemical signal of the aptasensor decreased. The electrochemical signal was recorded with a square wave voltammetry technical in the range of 0.5–250 ng/mL of SARS-CoV-2-RBD in a saliva sample. The limit of detection was found to be 0.36 ng/mL. Furthermore, the selectivity factor values of the proposed aptasensor to 32 ng/mL SARS-CoV-2-RBD in the presence of C-reactive protein, hemagglutinin, and neuraminidase of influenza A virus were 35.9, 11.7, and 17.37, respectively, indicating the high selectivity of the proposed aptasensor.

## 1. Introduction

Mesoporous silica nanomaterials is an inorganic nanomaterial that has several advantages such as small pore sizes (2–50 nm), high surface area, easy fabrication, and functionalization (Zhou et al., 2018). These advantages make the mesoporous silica nanomaterials a good candidate to be used for several purposes such as drug/gene delivery (Heidari et al., 2021; Zhou et al., 2018), nanomotor (Ma et al., 2015; Ma & Sanchez, 2015), energy conversion (Cheng et al., 2009; Zu et al., 2020), and sensing (Özalp et al., 2014; Shamsipur et al., 2017). Among them the sensing application of the mesoporous silica nanomaterials, the bio-gated mesoporous silica as a smart device has been used for the sensing of a wide range of biomolecules, opening a new chapter in the nano biosensing technology field. To fabricate the bio-gated mesoporous silica, a bio-recognizer such as enzymes (Chen et al., 2012), antibodies

(Climent et al., 2009), and aptamers (Zhang et al., 2014) are immobilized outside the pores of mesoporous silica as gatekeepers. However, the aptamer-gated mesoporous silica nanomaterials are the most favored ones due to their wide range of sensing applications like arsenite (Oroval et al., 2017), adenosine triphosphate (Özalp et al., 2014), DNA fragments of mycoplasma bacteria (Climent et al., 2013), thrombin (Oroval et al., 2013) detection. Inside the pores of the bio-gated mesoporous silica have been filled with probe molecules such as fluorescein (Qian et al., 2013), rhodamine b (Pascual et al., 2015), 3,3',5,5'-tetramethylbenzidine (Wang et al., 2014), tris(2,2'-bipyridyl)ruthenium(II) (Climent and Rurack, 2021), and methylene blue (MB) (Lee et al., 2020). In the presence of the relevant target, the gatekeepers of the mesoporous silica interact with its target, opening the pores (gates) of the bio-gated mesoporous silica. Consequently, the probe molecules release into the solution. The amount of the change in the signal of the probe molecule

\* Corresponding author.

\*\* Corresponding author.

E-mail addresses: [mahmoud.tabrizi@gmail.com](mailto:mahmoud.tabrizi@gmail.com), [mamouzad@ing.uc3m.es](mailto:mamouzad@ing.uc3m.es) (M. Amouzadeh Tabrizi), [pag@ing.uc3m.es](mailto:pag@ing.uc3m.es) (P. Acedo).

<https://doi.org/10.1016/j.bios.2022.114556>

Received 17 June 2022; Received in revised form 4 July 2022; Accepted 7 July 2022

Available online 16 July 2022

0956-5663/© 2022 Elsevier B.V. All rights reserved.

depends on the target concentration in the real sample (Climent et al., 2010; Ren et al., 2014). Since the electrochemical method can detect the biomarkers at trace levels (Aquino et al., 2022; Brazaca et al., 2022; Carr et al., 2020; Raymundo-Pereira et al., 2021; Soares et al., 2021), we decided to take the advantage of the bio-gated mesoporous silica nanomaterials and electrochemical method to fabricate a biosensor to detect the receptor-binding domain of severe acute respiratory syndrome coronavirus 2 (SARS-CoV-2-RBD). The SARS-CoV-2 that causes coronavirus disease-2019 (COVID-19) is a deadly virus. Hence, with a growing demand for the detection of COVID-19 in their early stages, in this research work, we have fabricated an electrochemical aptasensor for point-of-care detection of COVID-19 using the mesoporous silica film (MPSF). For this purpose, a laser engraved graphene electrode (LEGE) was first fabricated. The amino-functionalized MPSF was then fabricated electrochemically using silicon precursor (tetraethoxysilane, (3-aminopropyl)triethoxysilane, and template molecule (cetyltrimethylammonium bromide) on the surface of the LEGE. After that, the template molecule was removed to encapsulate the MB inside the MPSF (MB@MPSF). Consequently, the aptamer probes that could interact selectively with the SARS-CoV-2-RBD were immobilized on the surface of the mesoporous silica, generating an aptasensor (aptamer gated-MB@MPSF/LEGE). The aptamer probes that have a negative charge (due to their phosphate groups) are attracted by the positively charged MPSF (due to its amine groups), playing as the gatekeepers for the encapsulated MB (molecule probe) inside the pores. In the absence of the SARS-CoV-2-RBD, the electrochemical signal of the aptamer gated-MB@MPSF/LEGE was high because of the high presence of encapsulated MB inside the nanochannel of MPSF. As the real sample with a fixed level of the SARS-CoV-2-RBD was added to the surface of the aptamer gated-MB@MPSF/LEGE, the aptamer probes were removed on the surface of the MPSF to interact with SARS-CoV-2-RBD molecules and consequently, the encapsulated MB released to solution and washed away. Since the amount of the encapsulated MB inside the pores of the MPSF decreased, the electrochemical signal of the encapsulated MB decreased, indicating that the proposed detection method is a signal-off one. The fabricated aptamer gated-MB@MPSF/LEGE showed high selectivity, sensitivity, and stability.

## 2. Experimental section

### 2.1. Reagents and chemicals

Tetraethoxysilane (TEOS), (3-aminopropyl)triethoxysilane (APTS), cetyltrimethylammonium bromide (CTAB), potassium chloride (KCl), sodium chloride (NaCl), sodium nitrate ( $\text{NaNO}_3$ ), magnesium chloride ( $\text{MgCl}_2$ ), potassium ferricyanide ( $\text{K}_3[\text{Fe}(\text{CN})_6]$ ), potassium ferrocyanide ( $\text{K}_4[\text{Fe}(\text{CN})_6]$ ), MB, potassium dihydrogen phosphate ( $\text{KH}_2\text{PO}_4$ ), disodium hydrogen phosphate ( $\text{Na}_2\text{HPO}_4$ ), hydrochloric acid (HCl), acetic acid, tris hydrochloride (Tris-HCl), and ethanol were purchased from Cymit-Química (Barcelona, Spain). The aptamer probe (purified by HPLC) was purchased from Nzytech (Lisbon, Portugal). The aptamer sequence was: 5'-CAG CAC CGA CCT TGT GCT TTG GGA GTG CTG GTC CAA GGG CGT TAA TGG ACA-3' (Song et al., 2020). Hemagglutinin (HA), neuraminidase (NA), C-reactive protein (CRP), and SARS-CoV-2-RBD were obtained from Sigma-Aldrich (Louis, MO, USA). Syringe filters (0.22  $\mu\text{m}$ ) were obtained from Millipore-Sigma (Burlington, MA, USA). Kapton tape was obtained from Satkit (Tarragona, Spain).

The precursor solution for the fabrication of mesoporous silica film was prepared with TEOS (12.24 mmol), APTS (1.36 mmol) CTAB (4.35 mmol) in the mixture of  $\text{NaNO}_3$  (0.1 M, 20 mL), and ethanol (20 mL). The mixture was stirred for 150 min at pH 3 before fabricating the mesoporous silica film electrochemically.

The measuring buffer was a phosphate-buffered saline (PBS, 10 X or 0.1 M). 0.1 M PBS recipe contains 1.37 M NaCl, 27 mM KCl, 100 mM  $\text{Na}_2\text{HPO}_4$ , and 18 mM  $\text{KH}_2\text{PO}_4$ , pH 7.4. Aptamer solution (100  $\mu\text{M}$ ) was

made with 0.1 M PBS and 0.55 mM  $\text{MgCl}_2$ .

The hybridization buffer was prepared with 20 mM Tris-HCl, 10 mM KCl, and 37.5 mM  $\text{MgCl}_2$  with a pH fixed at 7.4.

### 2.2. Apparatus

The cyclic voltammetry (CV) and square wave voltammetry (SWV) studies were performed using a  $\mu\text{Stat}$  300 Bipotentiostat (Metrohm-DropSens, Spain). Transmission Electron Microscope (TEM) image were taken with a Philips Tecnai 20 FEG. The Fourier transform attenuated total reflectance spectrum (FT-ATR) study was performed by using Nicolet iS50 Fourier transform infrared spectrometer (Thermo Fisher Scientific, USA). The elemental analysis was performed using an energy dispersive analysis of X-rays (EDX) (EDAX, Mahwah, NJ, USA) and the data were analyzed with APEX software. A mini-peristaltic pump was purchased from Treedix (China). The three-dimensional (3D) image and surface profile were obtained from a two-dimensional (2D) image by the imageJ software. The LEGE and the flow cell fabrication process have been reported in our previous work (Amouzadeh Tabrizi and Acedo, 2022b). The geometric surface area ( $A_{\text{gsa}}$ ) of the working electrode was 0.125  $\text{cm}^2$ . The working, reference and counter electrodes were delimited from their connectors with a thin layer of transparent insulator ink. The working area that the solution must cover all these electrodes was isolated with a plastic O-ring in a flow cell setup.

The photo image of the LEGE during its fabrication and its SEM image was shown in Fig. S1.

### 2.3. Fabrication of the aptasensor

100  $\mu\text{L}$  of acetate buffer (0.1 M, pH 5.4) was first dropped on the surface of a LEGE and activated by potential sweeping between  $-1.0$  V and  $+1.5$  V at the scan rate of 0.1 V/s for 30 cycles. After that, the electrode was washed with distilled water and then put in a PBS and the potential was cycled between  $-1.0$  V and  $+1.0$  V at the scan rate of 0.1 V/s until a stable background signal of CV was obtained.

The MPSF/LEGE was then fabricated electrochemically by applying  $-1.3$  V for 20 s to a LEGE in a precursor solution (Walcarius et al., 2007). After that, the electrode was washed immediately with running distilled water for 5 min using a wash bottle. The electrode was then dried overnight in an oven at 130  $^\circ\text{C}$  followed by the surfactant removal step by moderate stirring in 0.1 M HCl/ethanol for 10 min.

The MPSF/LEGE was subsequently immersed in a 1 mM of MB solution (pH 7.4) under a moderate stirring condition for overnight at room temperature. The electrode was rinsed with deionized water to wash away the residual MB and then dried. 10  $\mu\text{L}$  of 100  $\mu\text{M}$  aptamer probe was then dropped onto the surface of the electrode and left for overnight at room temperature. During this period, the negatively charged phosphate groups of the aptamer probes were attracted to the positively charged amine groups on the MPSF via electrostatic attraction. Finally, the electrode was washed with 0.1 M PBS to remove the unbounded aptamer probe. The final electrode was named the aptamer gated-MB@MPSF/LEGE. The aptasensor was stored in a refrigerator (4  $^\circ\text{C}$ , in a dry box) when not in use. Fig. S2 shows a photo image of an aptamer/MB-MPSF/LEGE that was planted in a flow cell.

The schematic illustration of the fabrication process of the aptamer gated-MB@MPSF/LEGE employed is shown in Fig. 1.

### 2.4. Measurement process of SARS-CoV-2-RBD

2 mL of real saliva sample was filtered with a syringe filter (0.22  $\mu\text{m}$ ) to remove any microorganisms like bacteria. After that, 500  $\mu\text{L}$  of a real saliva sample was mixed with a 500  $\mu\text{L}$  hybridization buffer containing a fixed amount of SARS-CoV-2-RBD using a mini rotator for 5 min. The mixture was then pumped for 30 min to the flow cell where an aptamer gated-MB@MPSF/LEGE was planted in it. Since the interaction between the aptamer probe and target molecule (SARS-CoV-2-RBD) was higher

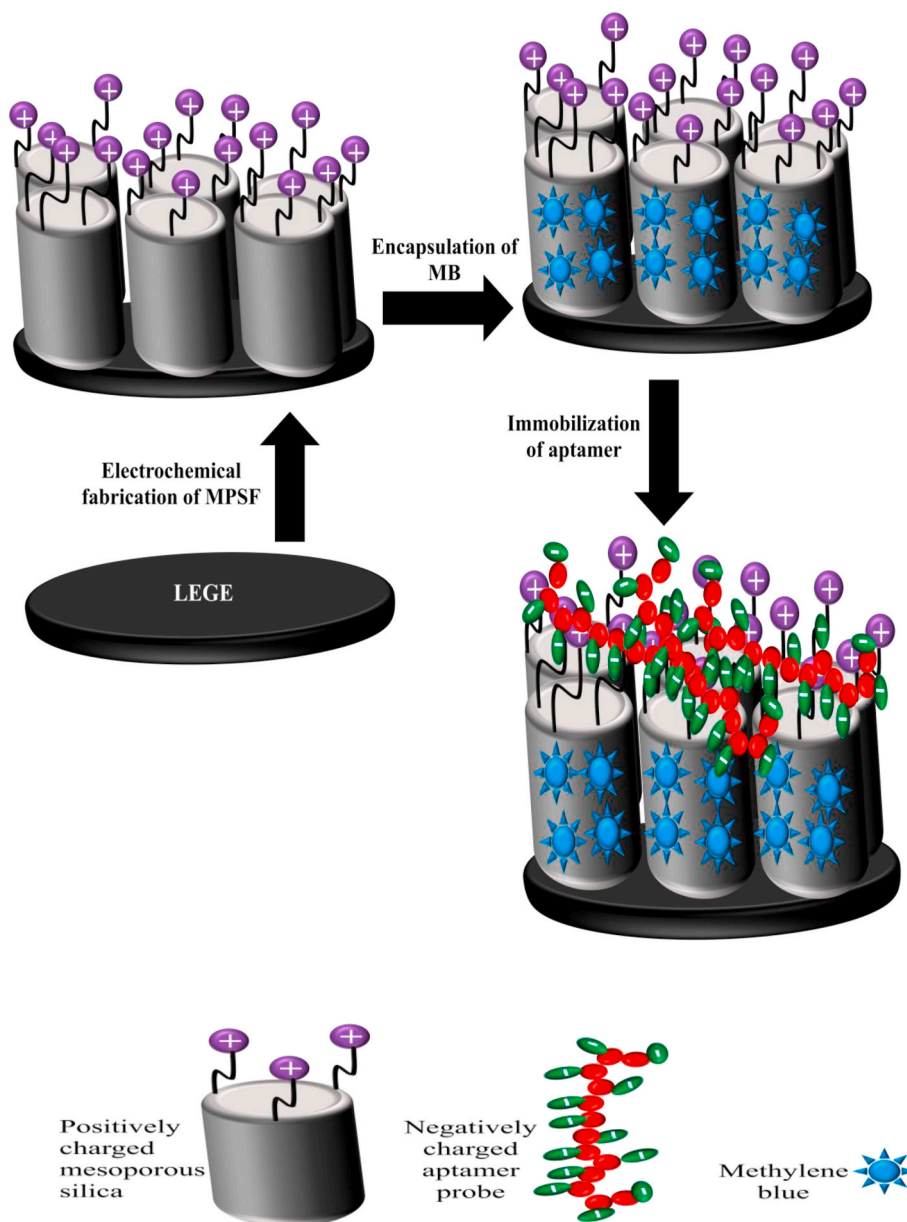


Fig. 1. The schematic illustration of fabrication steps for the aptamer-gated-MB@MPSF/LEGE.

than the electrostatic attraction between the negatively charged phosphate groups of the aptamer and the positively charged amino groups of the mesoporous silica film, the aptamer probes removed from the surface of mesoporous silica (Oroval et al., 2013) and subsequently, the MB desorbed into the solution and washed away with a measuring buffer (0.1 M PBS). Therefore, the electrochemical signal of the encapsulated MB decreased while the concentration of the SARS-CoV-2-RBD increased (Fig. S3).

### 3. Results and discussion

#### 3.1. Characterization of the nanostructured surface

Fig. 2 shows 2D (A) and 3D TEM (B) images, and the surface profile (C) of the MPSF. As it can be seen, the fabricated silica film had a porous structure. The average diameter of pore size is  $2.4 \text{ nm} \pm 0.2$  ( $n = 10$ ).

The elemental analysis of an aptamer-gated-MB@MPSF/LEGE was carried on by using EDX (Fig. 3A). As shown in this figure, a small peak at 0.4 keV related to nitrogen, a big peak at 0.5 keV related to oxygen

element, a small peak at a big peak at 1.7 keV related to silicon element (the backbone of MPSF), and a small peak at 2.15 keV related to phosphorous element (the backbone of aptamer probe) are clearly seen. A small peak at 0.3 keV related to carbon element of the MPSF and aptamer can be seen in the spectrum. Also, the peak at 0 keV is the noise peak caused by the electronics of the detector.

Fig. 3B shows the FT-ATR spectrum of the aptamer-gated-MB@MPSF/LEGE. As it can be seen, an absorption band at about  $3400 \text{ cm}^{-1}$  due to the  $-\text{NH}_2$  stretching,  $2930 \text{ cm}^{-1}$  and  $2900$  due to the  $-\text{CH}_x$  stretching, an absorption band at  $2300 \text{ cm}^{-1}$  due to the  $-\text{N-H}$  asymmetric stretching, an absorption band at  $1580$  due to the  $-\text{N-H}$  bending, absorption bands at  $1150 \text{ cm}^{-1}$  and  $926 \text{ cm}^{-1}$  due to the  $-\text{Si-O-Si}$  bending, the  $-\text{Si-OH}$ , respectively (Nechikkattu et al., 2019), an absorption band at  $1538 \text{ cm}^{-1}$  due to the  $-\text{C=O}$  stretching, an absorption band at  $1376 \text{ cm}^{-1}$  due to the  $-\text{C-N}$  stretching of amide III, an absorption band at  $1277 \text{ cm}^{-1}$  due to the  $-\text{PO}_2^-$  stretching in the aptamer probe, an absorption band at  $792 \text{ cm}^{-1}$  due to the  $=\text{C-H}$  bending, an absorption band at  $734 \text{ cm}^{-1}$  due to the  $-\text{C-S-C}$  bending (in the aromatic structure of MB) are clearly seen (Nowak et al., 2019).

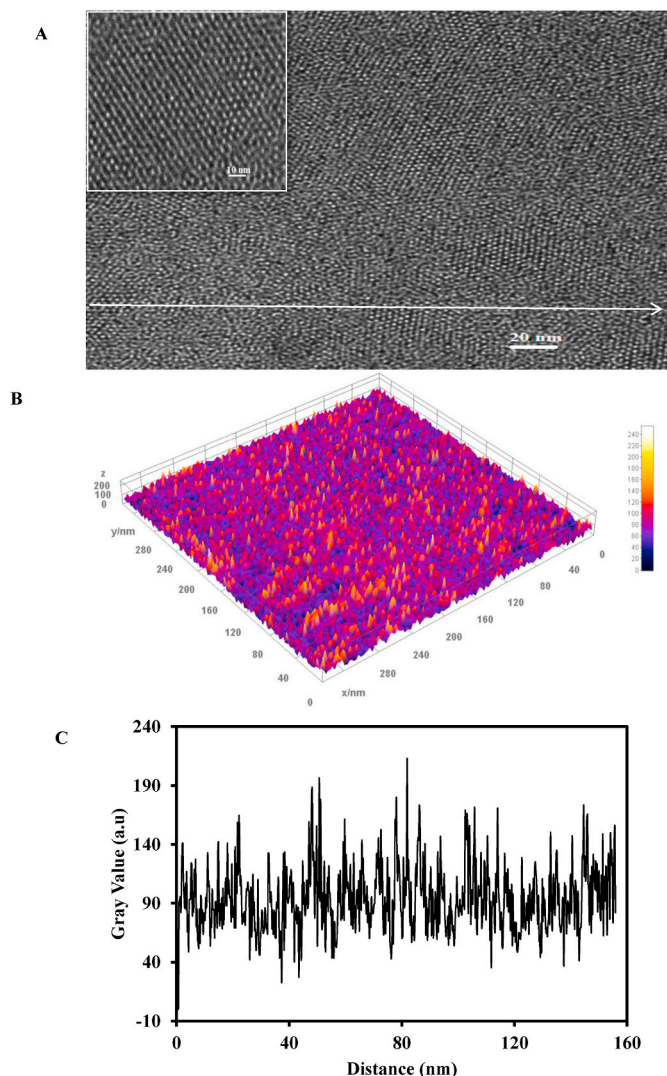


Fig. 2. (A) 2D and (B) 3D TEM images of the MPSF. (C) Surface profile of MPSF.

### 3.2. Electrochemical characterization of the aptamer gated-MB@MPSF/LEGE

Fig. S4 shows the CVs of the LEGE (a), and the MPSF/LEGE before (b) and after (c) the extraction of the template (CTAB) in a 0.1 M PBS containing 5.0 mM  $\text{Fe}(\text{CN})_6^{3-/4-}$  couple (1:1). As can be seen in Fig. S4 (a), a couple of well-defined and quasi-reversible redox peaks were recorded with a LEGE for  $\text{Fe}(\text{CN})_6^{3-/4-}$ . The intensities of the anodic ( $I_{pa}$ ) and cathodic ( $I_{pc}$ ) peak currents were +376  $\mu\text{A}$ , and -362  $\mu\text{A}$ , respectively, indicating that the LEGE could be used for electrochemical measurement purposes. However, after the electrochemical fabrication of the MPSF and before the extraction of CTAB, the peak intensities decreased dramatically ( $I_{pa} = +0.023 \mu\text{A}$ ,  $I_{pc} = -0.018 \mu\text{A}$ ) (b). It demonstrated the MPSF was fabricated on the surface of the LEGE, but the pores of the film were not opened yet. Therefore, the  $\text{Fe}(\text{CN})_6^{3-/4-}$  could not diffuse inside of the film. After the extraction of the CTAB, the peak intensities increased ( $I_{pa} = +116.4 \mu\text{A}$ ,  $I_{pc} = -118.9 \mu\text{A}$ ), indicating the pores were opened and the  $\text{Fe}(\text{CN})_6^{3-/4-}$  diffused into the film (c).

The CVs of the MPSF/LEGE (a) and aptamer gated-MB@MPSF/LEGE (b) in 0.1 M PBS (pH 7.4) are shown in Fig. 4A. As it can be seen, unlike the MPSF/LEGE, a couple of a pair of well-defined redox peaks of the MB was observed for the aptamer gated-MB@MPSF/LEGE. It indicated that

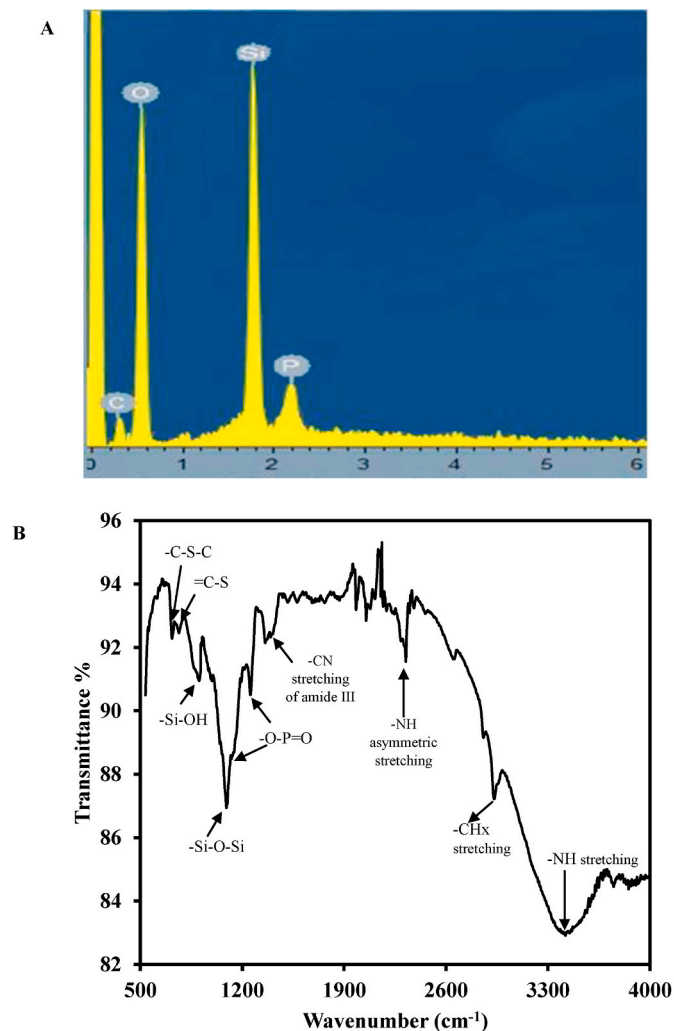


Fig. 3. (A) EDX and (B) FT-ATR spectrum of the aptamer gated-MB@MPSF/LEGE.

the MB molecules were encapsulated inside the MPSF/LEGE. The interday repeatability of the aptamer gated-MB@MPSF/LEGE was also studied under a multi-scan potential using the cyclic voltammetry technique (Fig. 4B). As shown, the CVs of the encapsulated MB in the aptamer gated-MB@MPSF/LEGE did not change, indicating that the MB did not release from the electrode to the solution. Fig. 4C shows the CVs of the aptamer gated-MB@MPSF/LEGE in the different scan rates in 0.1 M PBS (pH 7.4). As shown in Fig. 4D, the oxidation and reduction currents of MB have a linear relationship with the scan rate ( $\nu$ ) in the range of 0.01–0.15 V/s, revealing a surface-controlled for the encapsulated MB.

The surface concentration ( $\Gamma_c$ ) of the encapsulated MB was found to be 1.98  $\text{nmol}/\text{cm}^2$  from the integration of the anodic peak (Fig. S5) by using the equation (1):

$$Q = nF\Delta\Gamma_c \quad \text{eq (1)}$$

(Wang, 2006), where Q is the total faradaic charge of the anodic peak at the scan rate of 0.05 V/s (0.221 milli coulombs), n is the number of electrons ( $n = 2$ ), F is the Faraday constant of 96,485 C/mol, A that is the electroactive surface area of the MPSF/LEGE was found to be 0.51  $\text{cm}^2$  (the calculation process and related figures (Fig. S6) were included in the supporting data). Since the obtained  $\Gamma_c$  value for aptamer gated-MB@MPSF/LEGE was larger than the theoretical value for a monolayer immobilized MB ( $\Gamma_{\text{Theoretical}} = 0.220 \text{ nmol}/\text{cm}^2$ ) (Ju et al., 1995), therefore it indicated the MB molecules were immobilized in a 3D

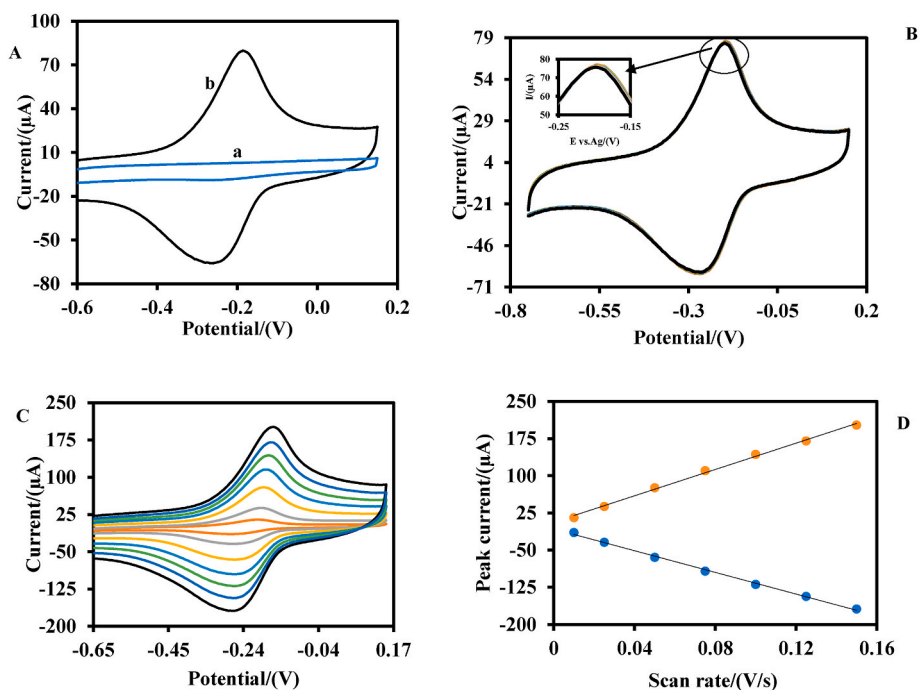


Fig. 4. (A) CVs of the MPSF/LEGE (a) and the aptamer gated-MB@MPSF/LEGE (b) in a PBS (0.1 M, pH 7.4) at a scan rate of 0.05 V/s. (B) Stability of the signal in a PBS (0.1 M, pH 7.4) at a scan rate of 0.05 V/s (C) CVs of the aptamer gated-MB@MPSF/LEGE in a PBS (0.1 M, pH 7.4) at various scan rates (0.01, 0.025, 0.05, 0.075, 0.1, 0.125, and 0.15 V/s from inner to outer). (D) The plot of the peak currents versus scan rate.

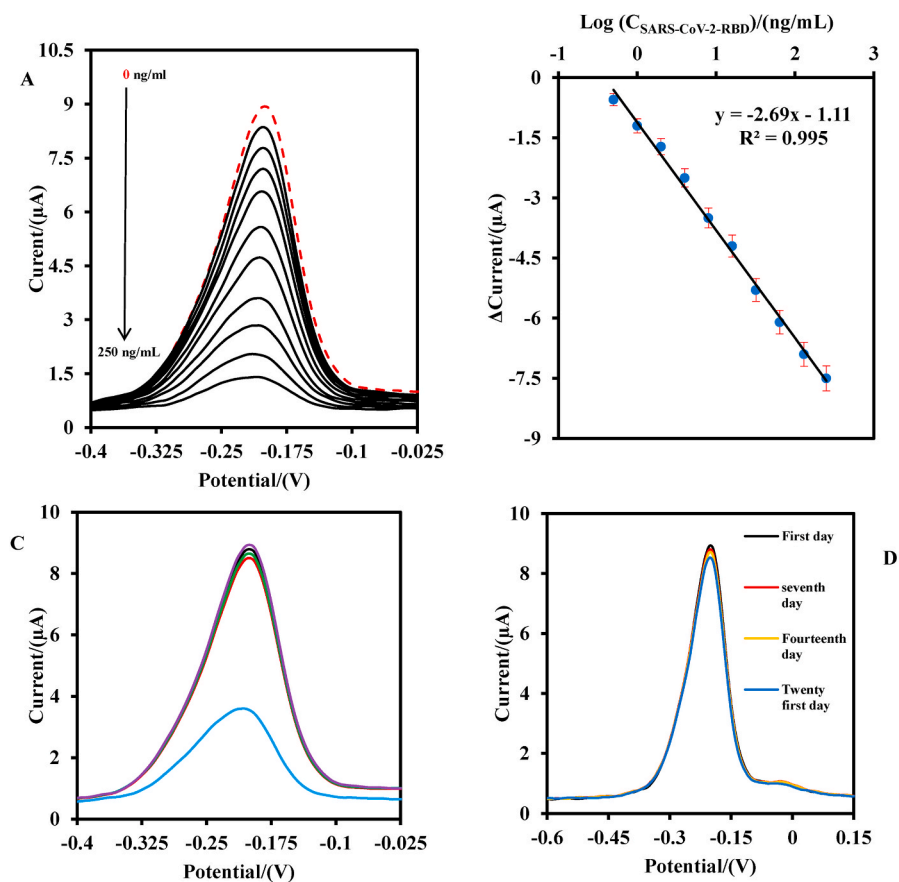


Fig. 5. (A) SWV of the aptamer gated-MB@MPSF/LEGE in a measuring buffer in the absence (brown dash curve) and presence of a fixed concentration of SARS-2-RBD (black dash curve). (B) The corresponding calibration plots of SWV response toward SARS-CoV-2-RBD (0.5, 1, 2.0, 4.0, 8.0, 16.0, 32.0, 64.0, 130.0, and 250.0 ng/mL). (C) The selectivity of an aptamer gated-MB@MPSF/LEGE to 32.0 ng/mL SARS-CoV-2 RBD (blue) in the absence (purple curve) and the presence of 32.0 ng/mL CRP (black curve), 32.0 ng/mL HA (red curve) and 32.0 ng/mL NA (green curve). (D) The stability of an aptamer gated-MB@MPSF/LEGE on the first day (black curve), seventh days (red curve), fourteenth days (yellow curve), and twenty-first days (blue curve).

nanostructure.

### 3.3. Voltammetric detection of SARS-CoV-2-RBD

Fig. 5 shows the SWV measurements (A), and logarithmic corresponding calibration plots (B) of the aptamer gated-MB@MPSF/LEGE to the different concentrations of SARS-CoV-2-RBD in the measuring buffer, respectively. As it can be seen, the response of the proposed aptasensor decreased as the concentration of SARS-CoV-2-RBD increased from 0.5 ng/mL to 250 ng/mL. Fig. 5B shows the calibration curve with a linear-logarithmic regression equation of  $\Delta I (\mu A) = -2.69 \text{ Log } C_{[ \text{SARS-CoV-2-RBD} ]} (\text{ng/mL}) - 1.11$  (eq 2). The limit of detection (LOD) of the proposed biosensor was found to be 0.36 ng/mL ( $3 \sigma/S$ ), where  $\sigma$  is the standard deviation of signal related to the blank solution (signals in the absence of SARS-CoV-2-RBD) and  $S$  is the slope of Fig. 5B. Since each SARS-CoV-2 has between 25 and 40 RBD (Highfield, 2020).

Therefore, the LOD of the aptamer gated-MB@MPSF/LEGE would be  $1.5\text{--}2.48 \times 10^8$  copies/mL using eq (3):

$$\text{Copies of virus/L} = \frac{\text{Molarity of SARS - CoV - 2 - RBD}}{\text{Number of RBD in aSARS - CoV - 2}} \times \text{Avogadro's number} \quad \text{eq (3)}$$

### 3.4. Selectivity and repeatability of the aptamer gated-MB@MPSF/LEGE

The selectivity of the aptamer gated-MB@MPSF/LEGE to 32 ng/mL of SARS-CoV-2-RBD was also investigated (Fig. 5C). To do that, the selectivity factor ( $\alpha$ ) was estimated by eq (4):

$$\alpha = \frac{(\frac{\Delta I}{I_0})_{\text{RBD}}}{(\frac{\Delta I}{I_0})_{\text{IA}}} \quad \text{eq (4)}$$

(Zhang et al., 2018), where  $(\Delta I/I_0)_{\text{RBD}}$  and  $(\Delta I/I_0)_{\text{IA}}$  are the normalized response of the aptamer gated-MB@MPSF/LEGE to the SARS-CoV-2-RBD and the interfering agents, respectively. The values of  $\alpha$  for the aptamer gated-MB@MPSF/LEGE to 32 ng/mL of SARS-CoV-2-RBD in the presence of the same concentrations of CRP, NA, and HA were 35.9, 17.37, 11.7, and, respectively. Since the values of  $\alpha$  were higher than one, therefore, the proposed aptasensor had a high selectivity to the SARS-CoV-2-RBD.

Furthermore, the inter-day repeatability (storage stability) of the aptamer gated-MB@MPSF/LEGE was studied every seven days for 21 days (Fig. 5D). The electrode was kept in a refrigerator ( $4^\circ\text{C}$ , in a dry box) and every seven its signal was recorded with the SWV method at a 0.1 M PBS. As it can be seen, the signal of the proposed aptasensor retained 95% of its original response after 21 days.

**Table 1**

Comparison of the analytical performance of the aptamer gated-MB@MPSF/LEGE with the other electrochemical aptasensors for the SARS-CoV-2-RBD detection.

Aptasensor	Electrochemical Method	Linear range	Limit of detection	Response time	Ref
Aptamer-MB/Gold electrode	SWV	10 pM –100 nM (0.35–3.5 ng/mL)	0.01 nM (0.35 ng/mL)	5 min	Idili et al. (2021)
Aptamer biotinylated/Au <sub>nano</sub> -MPA/SPE	DPV	10–50 ng/mL	2.63 ng/mL	40 min	Sari et al. (2022)
Aptamer/Yb-TCPP-4/Au NPs/GCE	PEC	0.5–8 μg/mL	72 ng/mL	70 min	Jiang et al. (2021)
Aptamer/Chitosan/CdS-gC3N4/ITO electrode	PEC	0.5–32.0 nM (17.5 ng/mL–1.12 μg/mL)	0.12 nM (4.2 ng/mL)	40 min	(Amouzadeh Tabrizi et al., 2021)
Aptamer/AuNP–CNF/CSPE	EIS	0.01–64 nM (0.35 ng/mL –2.24 μg/mL)	7 pM (0.24 ng/mL)	40 min	(Amouzadeh Tabrizi and Acedo, 2022a)
Aptamer/Au <sub>nano</sub> -S-Si-NPAAO/LEGE	SWV	2.5–40.0 ng/mL	0.8 ng/mL	20 min	(Amouzadeh Tabrizi and Acedo, 2022b)
MB-aptamer/SWCNT/SPE	DPV	20–100 nM	7 nM	120 min	Curti et al. (2022)
Aptamer gated-MB@MPSF/LEGE	SWV	0.5–250 ng/mL	0.36 ng/mL	30 min	This work

DPV: Differential pulse voltammetry; PEC: Photoelectrochemistry; GCE: Glassy carbon electrode; MPA: 3-Mercaptopropionic; SPE: Screen printed electrode; Au NPs: Gold nanoparticles; g-C<sub>3</sub>N<sub>4</sub>: Graphitic carbon nitride; CdS: Cadmium sulfide quantum dots; ITO: Indium tin oxide; EIS: Electrochemical impedance spectroscopy; Yb-TCPP-4: Two-dimensional metal-organic framework; Au<sub>nano</sub>-S-Si-NPAAO: Nanoporous anodic aluminium oxide silanized and decorated with gold nanoparticles; SWCNT: Single wall carbon nanotube.

The reproducibility was also studied with four different aptasensors (Fig. S7). As shown, no significant changes between the responses of the aptamer gated-MB@MPSF/LEGE were observed. It indicated that the aptamers were attracted to the surface of the MPSF strongly and consequently MB encapsulated inside the pores.

The analytical performances of the aptamer gated-MB@MPSF/LEGE such as linear response range, the limit of detection, and response time of it have been compared with the other electrochemical aptasensors for the SARS-CoV-2-RBD detection (Table 1). As it can be seen, only the labeled-based aptasensor that has been reported by Merkoçi's group has slightly better performances (Idili et al., 2021). However, the response range of their proposed aptasensor is limited. Also, the labeled aptamers are more expensive than the labeled free ones that we used in this research work.

The responses of the aptamer gated-MB@MPSF/LEGE to 1 ng/mL and 130 ng/mL of SARS-CoV-2-RBD were compared with the responses of the ELISA kit as a standard method. As shown in Table S1, the P values were higher than 0.05, indicating that responses of the aptamer gated-MB@MPSF/LEGE were not statistically significant differences from the ELISA kit.

## 4. Conclusions

In summary, an electrochemical biosensor was fabricated for the SARS-CoV-2-RBD detection in saliva sample by using mesoporous silica film as a nano-container to load the MB as a probe molecule and an aptamer probe as a gatekeeper to cap the mesoporous silica film. The electrostatic attraction between the aminated mesoporous silica film and aptamer probe encapsulated the MB inside the film. Since the interaction of the aptamer probe with the SARS-CoV-2-RBD was stronger than the electrostatic attraction, the MB molecules released from the film to the solution as SARS-CoV-2-RBD molecules were in the real sample. The proposed biosensor showed several advantages such as a wide response range, low detection limit, high selectivity, fast response, and low cost, making it an alternative method to the ELISA method in situations where all equipments needed for diagnosis are not available or financial predicament. The proposed aptasensor provided an opportunity for the point-of-care diagnosis of COVID-19.

### CRedit authorship contribution statement

**Mahmoud Amouzadeh Tabrizi:** Conceptualization, Methodology, Data curation, Formal analysis, Validation, Investigation, Visualization, Writing – original draft, Resources, Project administration, Funding acquisition. **Pablo Acedo:** Writing – review & editing.

## Declaration of competing interest

The authors declare that they have no known competing financial interests or personal relationships that could have appeared to influence the work reported in this paper.

## Data availability

Data will be made available on request.

## Acknowledgments

This project received funding from the European Union's Horizon 2020 research and innovation program under the Marie Skłodowska-Curie grant agreement No 801538, the Community of Madrid within the framework of the multi-year agreement with Universidad Carlos III Madrid in its line of action "Excellence for University Teaching Staff" V Regional Plan for Scientific Research, and Technological Innovation 2016–2020, and by the Programa de Actividades de I + D entre Grupos de Investigación de la Comunidad de Madrid, S2018/BAA-4480, Bioplictec-CM.

## Appendix A. Supplementary data

Supplementary data to this article can be found online at <https://doi.org/10.1016/j.bios.2022.114556>.

## References

- Amouzadeh Tabrizi, M., Acedo, P., 2022a. *Biosensors* 12 (3), 142.
- Amouzadeh Tabrizi, M., Acedo, P., 2022b. *Appl. Surf. Sci.* 598, 153867.
- Amouzadeh Tabrizi, M., Nazari, L., Acedo, P., 2021. *Sensor. Actuator. B Chem.* 345, 130377.
- Aquino, A., Paschoalin, V.M.F., Tessaro, L.L.G., Raymundo-Pereira, P.A., Conte-Junior, C.A., 2022. *J. Pharm. Biomed. Anal.* 211, 114608.
- Brazaca, L.C., Imamura, A.H., Gomes, N.O., Almeida, M.B., Scheidt, D.T., Raymundo-Pereira, P.A., Oliveira, O.N., Janegitz, B.C., Machado, S.A.S., Carrilho, E., 2022. 1, 1–11.
- Carr, O., Raymundo-Pereira, P.A., Shimizu, F.M., Sorroche, B.P., Melendez, M.E., de Oliveira Pedro, R., Miranda, P.B., Carvalho, A.L., Reis, R.M., Arantes, L.M.R.B., Oliveira, O.N., 2020. *Talanta* 210, 120609.
- Chen, M., Huang, C., He, C., Zhu, W., Xu, Y., Lu, Y., 2012. *Chem. Commun.* 48 (76), 9522–9524.
- Cheng, S.-H., Lee, C.-H., Yang, C.-S., Tseng, F.-G., Mou, C.-Y., Lo, L.-W., 2009. *J. Mater. Chem.* 19 (9), 1252–1257.
- Climent, E., Bernardos, A., Martínez-Máñez, R., Maquieira, A., Marcos, M.D., Pastor-Navarro, N., Puchades, R., Sancenón, F., Soto, J., Amorós, P., 2009. *J. Am. Chem. Soc.* 131 (39), 14075–14080.
- Climent, E., Martínez-Máñez, R., Sancenón, F., Marcos, M.D., Soto, J., Maquieira, A., Amorós, P., 2010. *Angew. Chem. Int. Ed.* 49 (40), 7281–7283.
- Climent, E., Mondragón, L., Martínez-Máñez, R., Sancenón, F., Marcos, M.D., Murguía, J. R., Amorós, P., Rurack, K., Pérez-Payá, E., 2013. *Angew. Chem. Int. Ed.* 52 (34), 8938–8942.
- Climent, E., Rurack, K., 2021. *Angew. Chem. Int. Ed.* 60 (50), 26287–26297.
- Curti, F., Fortunati, S., Knoll, W., Giannetto, M., Corradini, R., Bertucci, A., Careri, M., 2022. *ACS Appl. Mater. Interfaces* 14 (17), 19204–19211.
- Heidari, R., Khosravian, P., Mirzaei, S.A., Elahian, F., 2021. *Sci. Rep.* 11 (1), 20531.
- Highfield, R., 2020. <https://www.sciencemuseumgroup.org.uk/blog/coronavirus-the-spike/>.
- Idili, A., Parolo, C., Alvarez-Diduk, R., Merkoçi, A., 2021. *ACS Sens.* 6 (8), 3093–3101.
- Jiang, Z.W., Zhao, T.T., Li, C.M., Li, Y.F., Huang, C.Z., 2021. *ACS Appl. Mater. Interfaces* 13 (42), 49754–49761.
- Ju, H., Zhou, J., Cai, C., Chen, H., 1995. *Electroanalysis* 7 (12), 1165–1170.
- Lee, I., Kim, S.-E., Lee, J., Woo, D.H., Lee, S., Pyo, H., Song, C.-S., Lee, J., 2020. *Biosens. Bioelectron.* 152, 112010.
- Ma, X., Hahn, K., Sanchez, S., 2015. *J. Am. Chem. Soc.* 137 (15), 4976–4979.
- Ma, X., Sanchez, S., 2015. *Chem. Commun.* 51 (25), 5467–5470.
- Nechikkattu, R., Park, S.S., Ha, C.-S., 2019. *Microporous Mesoporous Mater.* 279, 117–127.
- Nowak, E., Wisła-Świder, A., Khachatryan, G., Fiedorowicz, M., Danel, K., 2019. *Eur. Biophys. J.* 48 (4), 371–381.
- Oroval, M., Climent, E., Coll, C., Eritja, R., Aviñó, A., Marcos, M.D., Sancenón, F., Martínez-Máñez, R., Amorós, P., 2013. *Chem. Commun.* 49 (48), 5480–5482.
- Oroval, M., Coll, C., Bernardos, A., Marcos, M.D., Martínez-Máñez, R., Shchukin, D.G., Sancenón, F., 2017. *CS Appl. Mater. Interfaces* 9 (13), 11332–11336.
- Özalp, V.C., Pinto, A., Nikulina, E., Chuvilín, A., Schäfer, T., 2014. *Part. Part. Syst. Char.* 31 (1), 161–167.
- Pascual, L., Baroja, I., Aznar, E., Sancenón, F., Marcos, M.D., Murguía, J.R., Amorós, P., Rurack, K., Martínez-Máñez, R., 2015. *Chem. Commun.* 51 (8), 1414–1416.
- Qian, R., Ding, L., Ju, H., 2013. *J. Am. Chem. Soc.* 135 (36), 13282–13285.
- Raymundo-Pereira, P.A., de Oliveira Pedro, R., Carr, O., Melendez, M.E., Gobbi, A.L., Helena de Oliveira Piazzetta, M., Carvalho, A.L., Reis, R.M., Miranda, P.B., Oliveira, O.N., 2021. *J. Phys. Chem. C* 125 (1), 498–506.
- Ren, K., Wu, J., Zhang, Y., Yan, F., Ju, H., 2014. *Anal. Chem.* 86 (15), 7494–7499.
- Sari, A.K., Hartati, Y.W., Gaffar, S., Anshori, I., Hidayat, D., Wiraswati, H.L., 2022. *J. Electrochem. Sci. Eng.* 21 (1), 219–235.
- Shamsipur, M., Karimi, Z., Amouzadeh Tabrizi, M., Rostamnia, S., 2017. *J. Electroanal. Chem.* 799, 406–412.
- Soares, J.C., Soares, A.C., Rodrigues, V.C., Oiticica, P.R.A., Raymundo-Pereira, P.A., Bott-Neto, J.L., Buscaglia, L.A., de Castro, L.D.C., Ribas, L.C., Scabini, L., Brazaca, L.C., Correa, D.S., Mattoso, L.H.C., de Oliveira, M.C.F., de Carvalho, A.C.P.L.F., Carrilho, E., Bruno, O.M., Melendez, M.E., Oliveira, O.N., 2021. *Mater. Chem. Front.* 5 (15), 5658–5670.
- Song, Y., Song, J., Wei, X., Huang, M., Sun, M., Zhu, L., Lin, B., Shen, H., Zhu, Z., Yang, C., 2020. *Anal. Chem.* 92 (14), 9895–9900.
- Walcarius, A., Sibottier, E., Etienne, M., Ghanbaja, J., 2007. *Nat. Mater.* 6 (8), 602–608.
- Wang, J., 2006. *Analytical Electrochemistry*. VCH, New York.
- Wang, Z., Yang, X., Feng, J., Tang, Y., Jiang, Y., He, N., 2014. *Analyst* 139 (23), 6088–6091.
- Zhang, L., Wang, G., Xiong, C., Zheng, L., He, J., Ding, Y., Lu, H., Zhang, G., Cho, K., Qiu, L., 2018. *Biosens. Bioelectron.* 105, 121–128.
- Zhang, Z., Wang, F., Balogh, D., Willner, I., 2014. *J. Mater. Chem. B* 2 (28), 4449–4455.
- Zhou, Y., Quan, G., Wu, Q., Zhang, X., Niu, B., Wu, B., Huang, Y., Pan, X., Wu, C., 2018. *Acta Pharm. Sin.* B. 8 (2), 165–177.
- Zu, L., Zhang, W., Qu, L., Liu, L., Li, W., Yu, A., Zhao, D., 2020. *Adv. Energy Mater.* 10 (38), 2002152.